PHOTONICS Research

Ultra-sensitive Dirac-point-based biosensing on terahertz metasurfaces comprising patterned graphene and perovskites

Xin Yan,[1,†] Tengteng Li,[2,†] Guohong Ma,[3] Ju Gao,[1] Tongling Wang,[4] Haiyun Yao,[1,6] Maosheng Yang,[5,7] Lanju Liang,[1,8] Jing Li,[5] Jie Li,[2] Dequan Wei,[1] Meng Wang,[1] Yunxia Ye,[5] Xiaoxian Song,[5] Haiting Zhang,[5] Chao Ma,[5] Yunpeng Ren,[5] Xudong Ren,[5] and Jianquan Yao[2]

[1]School of Opto-electronic Engineering, Zaozhuang University, Zaozhuang 277160, China
[2]College of Precision Instruments and Opto-electronics Engineering, Tianjin University, Tianjin 300072, China
[3]Department of Physics, School of Science, Shanghai University, Shanghai 200444, China
[4]School of Telecommunications, Qilu University of Technology, Jinan 250306, China
[5]Institute of Micro-nano Optoelectronics and Terahertz Technology, College of Information Science and Engineering, Jiangsu University, Zhenjiang 212013, China
[6]e-mail: haiyun1990yao@163.com
[7]e-mail: 2111803010@stmail.ujs.edu.cn
[8]e-mail: lianglanju123@163.com

Received 24 September 2021; revised 7 November 2021; accepted 18 November 2021; posted 18 November 2021 (Doc. ID 444225); published 7 January 2022

Biosensors are a focus of research on terahertz metasurfaces. However, reports of ultra-sensitive biosensors based on Dirac points are rare. Here, a new terahertz metasurface is proposed that consists of patterned graphene and perovskites. This serves as an ultra-sensitive Dirac-point-based biosensor for qualitative detection of sericin. Theoretically, sericin may make graphene n-doped and drive the Fermi level to shift from the valence band to the Dirac point, causing a dramatic decrease in conductivity. Correspondingly, the dielectric environment on the metasurface undergoes significant change, which is suited for ultra-sensitive biosensing. In addition, metal halide perovskites, which are up-to-date optoelectronic materials, have a positive effect on the phase during terahertz wave transmission. Thus, this sensor was used to successfully detect sericin with a detection limit of 780 pg/mL, achieved by changing the amplitude and phase. The detection limit of this sensor is as much as one order of magnitude lower than that of sensors in published works. These results show that the Dirac-point-based biosensor is a promising platform for a wide range of ultra-sensitive and qualitative detection in biosensing and biological sciences.

https://doi.org/10.1364/PRJ.444225

1. INTRODUCTION

A metasurface is a 2D artificial metamaterial composed of periodic sub-wavelength geometric unit cells [1–7]. Its coupling with electromagnetic waves generates a unique resonant response with far-ranging applications to modern photonic devices such as modulators [8–10], absorbers [11,12], lenses [13], and sensors [14–17]. Recently, the plasmonic analog of electromagnetically induced transparency (EIT) has been generated in sub-wavelength geometric structures [18,19]. The absorbance linewidth is limited only by Drude damping, and the narrow EIT-like features render it ideal for biosensors [20]. Attempts have been made to realize ultra-sensitivity with EIT-like metasurface-based biosensors. However, related reports are rare owing to difficulties in changing the dielectric environment. A metasurface with graphene and metal halide perovskites may solve this problem. In such a device, graphene and metal halide perovskites work together to produce a resonant response that is ultra-sensitive to change in the dielectric environment under an external stimulus.

Graphene is a two-dimensional atomic system [21,22]. It allows modification of the Fermi level (E_F) and the corresponding charge carrier density through biological, electrical, and optical methods [8,23,24]. Chemical vapor deposition (CVD) is a conventional method for producing graphene [25]. However, it is inevitably affected by impurities, defects, and disorders. CVD-graphene is usually p-doped, so the initial E_F slightly deviates from the Dirac point and is in the valence band. In other words, the initial E_F is quite close to the Dirac point [26]. The E_F requires extremely weak external stimuli to move from the valence band to the Dirac point [27], which is suitable

for an ultra-sensitive biosensor. Patterned graphene devices have also been widely researched for use in modern advanced equipment [28]. Patterning is the key to manufacturing graphene devices. Patterning graphene on the micro/nanoscale may greatly improve the performance of optical devices, which benefit from low-loss plasma characteristics [29]. Therefore, the patterning of graphene is an important factor that affects device performance [30]. Therefore, CVD-patterned graphene is ideal for producing an ultra-sensitive Dirac-point-based biosensor and tunable optics devices.

Metal halide perovskites are up-to-date optoelectronic materials with the crystal formula ABX_3 [A = CH_3NH_3 (MA), $CH(NH_2)_2$ (FA), Cs; B = Pb, Sn; X = Cl, Br, I] [31–35]. In recent years, perovskites have shown great advantages in optics devices. Examples include photodetectors, solar cells, light-emitting diodes, and optical modulators [36–38]. The excellent optoelectronic properties of metal halide perovskites have received great attention from the optics community. Most importantly, a metal halide perovskite has a high and adjustable relative permittivity that exerts a greater influence on the phase of a terahertz wave passing through it, which plays an active role in phase-based sensors.

In this work, a hybrid dual-optoelectronic-material terahertz metasurface (HDOMM) is used for a Dirac-point-based biosensor. The HDOMM contains an EIT-like metasurface and a sandwich complex composed of graphene, polyimide (PI), and a metal halide perovskite. The HDOMM is used as a platform for ultra-sensitive and qualitative detection of sericin. Using the changes in amplitude and phase, HDOMM can detect sericin with a detection limit of 780 pg/mL. The internal mechanism for ultra-sensitive sensing includes the following two aspects. First, the sericin drives the E_F of graphene to move to the Dirac point, causing a dramatic change in the dielectric environment. This is the main factor. Second, a metal halide perovskite boosts the positive effect on the phase. This plays a secondary role. These two factors are used to achieve ultra-sensitive label-free sensing with the HDOMM.

2. RESULTS AND DISCUSSION

A. Fabrication of the HDOMM and Its Characteristics

As shown in Fig. 1(a), the manufacturing process begins with the preparation of an EIT-like metasurface. The unit cell consists of a cut-wire resonator (CW) and two split-oval-ring resonators (SORRs). These resonators were engineered through conventional photolithography [Fig. 1a(i)]. Then, an $MAPbI_3$ film was spin-coated on the metasurface [Fig. 1a(ii)]. The $MAPbI_3$ wrapped the CWs and SORRs with good uniformity. Next, the $MAPbI_3$ was covered with a 1.5-μm-thick PI film [Fig. 1a(iii)]. PI was used to completely isolate $MAPbI_3$ from the ambient conditions, conferring stability to the $MAPbI_3$. After that, trilayer graphene was transferred onto the PI film [Fig. 1a(iv)].

Subsequently, the graphene was patterned into a fishing net structure with round holes whose diameters are 100 μm [Fig. 1a(v, vi)]. Figure 1(b) shows optical microscope images of the bare EIT-like metasurface, the EIT-like metasurface with graphene and $MAPbI_3$, and the EIT-like metasurface with patterned graphene and $MAPbI_3$. Finally, the HDOMM was used as a Dirac-point-based biosensor [Fig. 1a(vi)]. The dimensions of the unit cell and the electric and magnetic boundary conditions are shown in Fig. 1(c). Figure 1(d) displays the Raman spectrum of graphene excited by a 514-nm laser. The D peak has disappeared. The 2D peak is located at 2680 cm^{-1}, and the G peak is at 1600 cm^{-1}. The intensity of the 2D peak is lower than that of the G peak. In addition, the full width at half-maximum of the 2D peak is ~55 cm^{-1}. These results show that the graphene has high quality. Before the X-ray diffraction (XRD) measurement, an $MAPbI_3$ film was deposited on a silicon substrate. Figure 1(e) shows the XRD spectrum. The diffraction peaks are at 14.34°, 28.72°, and 32.16°, representing the (110), (220), and (310) crystal planes, respectively. Figure 1(e) shows no characteristic peaks associated with PbI_2 and other redundant phases. The inset of Fig. 1(e) is the top-view SEM image of the $MAPbI_3$ film. The $MAPbI_3$ film has large grains and no pinholes, demonstrating a smooth, uniform morphology.

B. Mechanism of EIT-Like Metasurface and Theoretical Model

Figure 2(a) shows the experiment and simulation transmission spectra of the bare EIT-like metasurface, which presents a classic W-line shape. The experiment results agree relatively well with the simulation results in Fig. 2(a). However, there are still some differences due to the inevitable errors in processing and measuring. Figure 2(c) shows the simulated electric field distributions at 0.65 THz. For the CW, the electric field demonstrates a dipole resonant mode acting as a bright mode. Because the CW couples the incident THz waves, the electric field of the CW is consistently oriented in the polarization direction of the THz waves [39,40], whereas the SORRs decouple from the incident THz waves, serving as a dark mode. However, when the incident THz waves excite the CW, the dark mode couples with the bright mode. Figure 2(c) shows that the electric field of two SORRs is opposite that of the CW. This indicates a coupling with the near field of the CW. Because the CW and SORRs keep comparable excitation strength and a π phase difference, there is destructive interference between the bright and dark modes, which causes a narrow transparency window [40,41]. The coupled harmonic oscillator model is applied to describe the destructive interference between the bright and dark modes. The interference can be analytically described by the coupled differential equations [39–41]

$$\begin{aligned} \ddot{x}_1 + \gamma_1\dot{x}_1 + \omega_0^2 x_1 + \kappa x_2 &= E, \\ \ddot{x}_2 + \gamma_2\dot{x}_2 + (\omega_0 + \delta)^2 x_2 + \kappa x_1 &= 0, \end{aligned} \tag{1}$$

where x_1 and x_2 are the resonant amplitudes, and γ_1 and γ_2 the losses of bright and dark modes, respectively; δ is the detuning of the resonant frequency of the dark-mode oscillator from the bright-mode one; and κ is the coupling coefficient between the two oscillators. Solving Eq. (1) with the approximation $\omega - \omega_0 \ll \omega_0$ yields the susceptibility χ:

$$\chi = \chi_r + i\chi_i \propto \frac{(\omega - \omega_0 - \delta) + i\frac{\gamma_2}{2}}{(\omega - \omega_0 + i\frac{\gamma_1}{2})(\omega - \omega_0 - \delta + i\frac{\gamma_2}{2}) - \frac{\kappa^2}{4}}. \tag{2}$$

The energy loss is always proportional to the imaginary part of χ; thus, the transmission can be written as

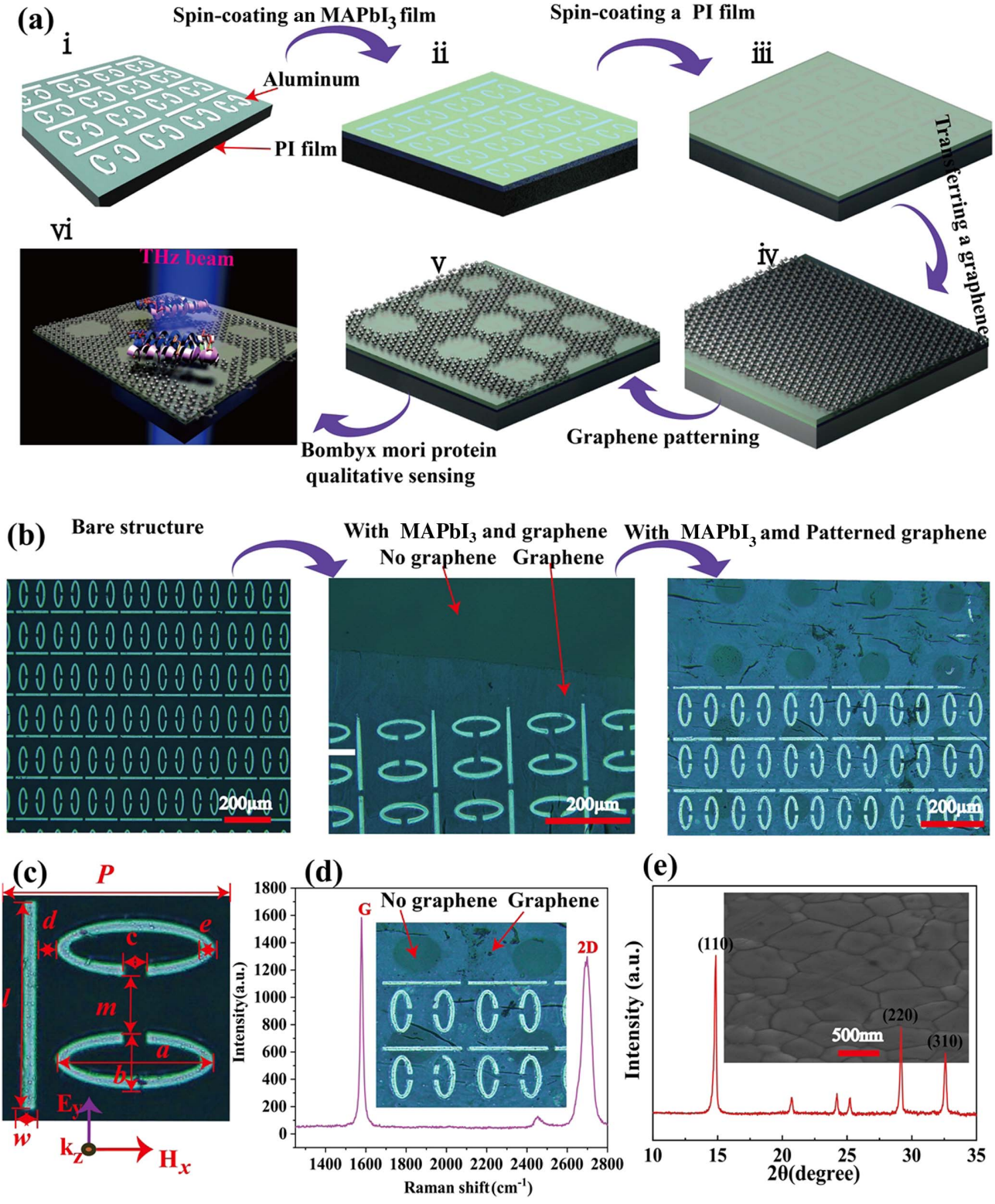

Fig. 1. Manufacture and characterization of the HDOMM. (a) Manufacturing process: (i) an EIT-like metasurface sample was prepared; (ii) a metal halide perovskite [$CH_3NH_3PbI_3$ ($MAPbI_3$)] was spin-coated on the EIT-like metasurface sample; (iii) the PI film was spin-coated on $MAPbI_3$; (iv) graphene was transferred onto the PI film; (v) the trilayer graphene was patterned into a fishing net structure with round holes; (vi) sericin was qualitatively sensed. (b) Three optical microscope images of the different samples. (c) Unit cell of the EIT-like metasurface. The corresponding parameters are $P = 200$ μm, $l = 170$ μm, $w = 20$ μm, $a = 130$ μm, $b = 60$ μm, $c = 40$ μm, $d = 15$ μm $e = 10$ μm, $m = 36$ μm. (d) Raman spectrum of graphene. The inset is a sample of the EIT-like metasurface with the patterned graphene and $MAPbI_3$ film. (e) X-ray diffraction (XRD) pattern of the perovskite films. The inset is an SEM image of $MAPbI_3$.

$$T \propto 1 - \chi_i = 1 - g\chi_i, \tag{3}$$

where χ_i is the imaginary part of the susceptibility, which is proportional to the energy loss. The transmission T is calculated from $T = 1 - g\chi_i$, in which g is the geometric parameter describing the strength of the coupling of the bright mode with the incident electric field $\boldsymbol{E}$. During coupling, the absorbance linewidth is limited only by Drude damping. That is to say, any change in the transparency window is due only to the external dielectric environment owing to the suppression of radiative losses [20]. In addition, Fig. 2(d) shows circulating current distributions along SORRs, representing low radiation loss. Therefore, the excellent features render the EIT-like metasurface ideal for biosensors.

To realize ultra-sensitive sensing, the HDOMM was used as a platform for qualitative detection of sericin, which has strong water solubility. For such detection, the patterned graphene is in direct contact with the sericin and performs the main sensing function. The perovskite is not in direct contact with the sericin, boosting the influence on the phase. This plays a secondary role. The change in the dielectric environment is mainly due to the conductivity of the patterned graphene. Therefore, the relationship between the conductivity and transmission spectra of the HDOMM was simulated to clarify the sensing mechanism of the HDOMM. Figure 2(b) shows the simulated transmission spectra under different conductivities. The transparency window gradually shrinks with increasing conductivity. An in-depth understanding of the electromagnetic behavior is

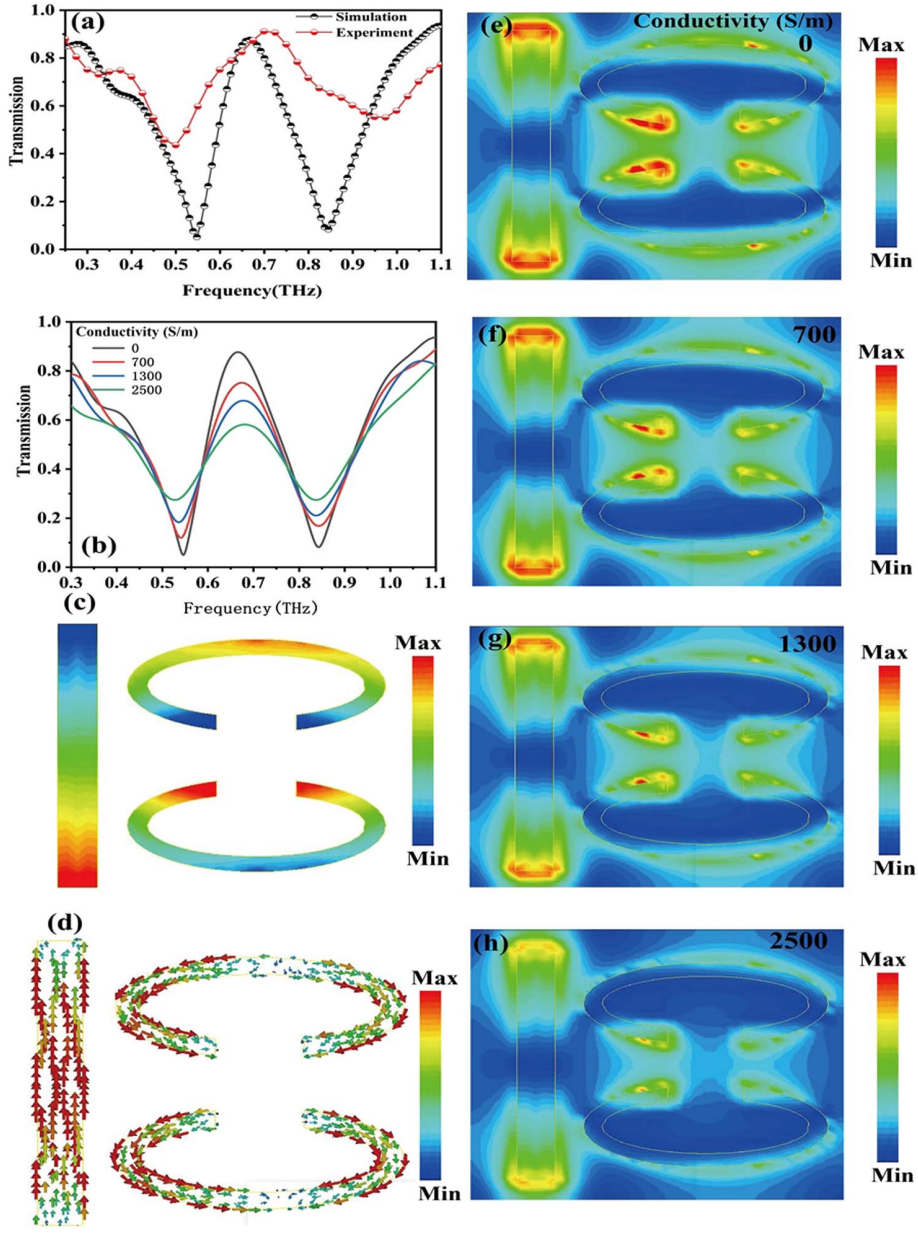

Fig. 2. Performance and mechanism of the EIT-like metasurface. (a) Experimental and simulated transmission spectra. (b) Simulated transmission spectra under different conductivities. (c) Simulated electric field distributions at 0.65 THz. (d) Surface current distributions at 0.65 THz. (e)–(h) Simulated electric field distributions under different conductivities.

obtained from the simulated electric field distributions in Figs. 2(e)–2(h) for the HDOMM under different conductivities. The field concentrations are strong when the conductivity is 0 S/m [Fig. 2(i)]. However, as the conductivity increases from 0 to 2500 S/m, the electric fields gradually decrease. Correspondingly, the transparency window shrinks.

C. HDOMM Application to Sericin Sensing

Figures 3(a)–3(c) show the experimental transmission spectra for the HDOMM at sericin concentrations from 780 pg/mL to 1.25 μg/mL. Compared with that of the bare HDOMM, the transparency window with sericin is significantly enhanced. The obvious enhancement of the transparency window facilitates well the qualitative sensing of sericin. To clarify the sensing effect further, it is defined as $\Delta T/T = [(T_{\text{sericin}} - T_{\text{bare}})/T_{\text{bare}}] \times 100\%$, where T_{sericin} (T_{bare}) is the transmittance at the transparency window with (without) sericin. From Figs. 3(a)–3(c), $\Delta T/T$ for sericin at 1.25 μg/mL (highest concentration) is 6.7%, slightly higher than $\Delta T/T = 5.0\%$ at 1.17 ng/mL; however, this is much lower than $\Delta T/T = 21\%$ for sericin at 780 pg/mL (lowest concentration). The conclusion drawn from these results is that the HDOMM can serve as an ultra-sensitive

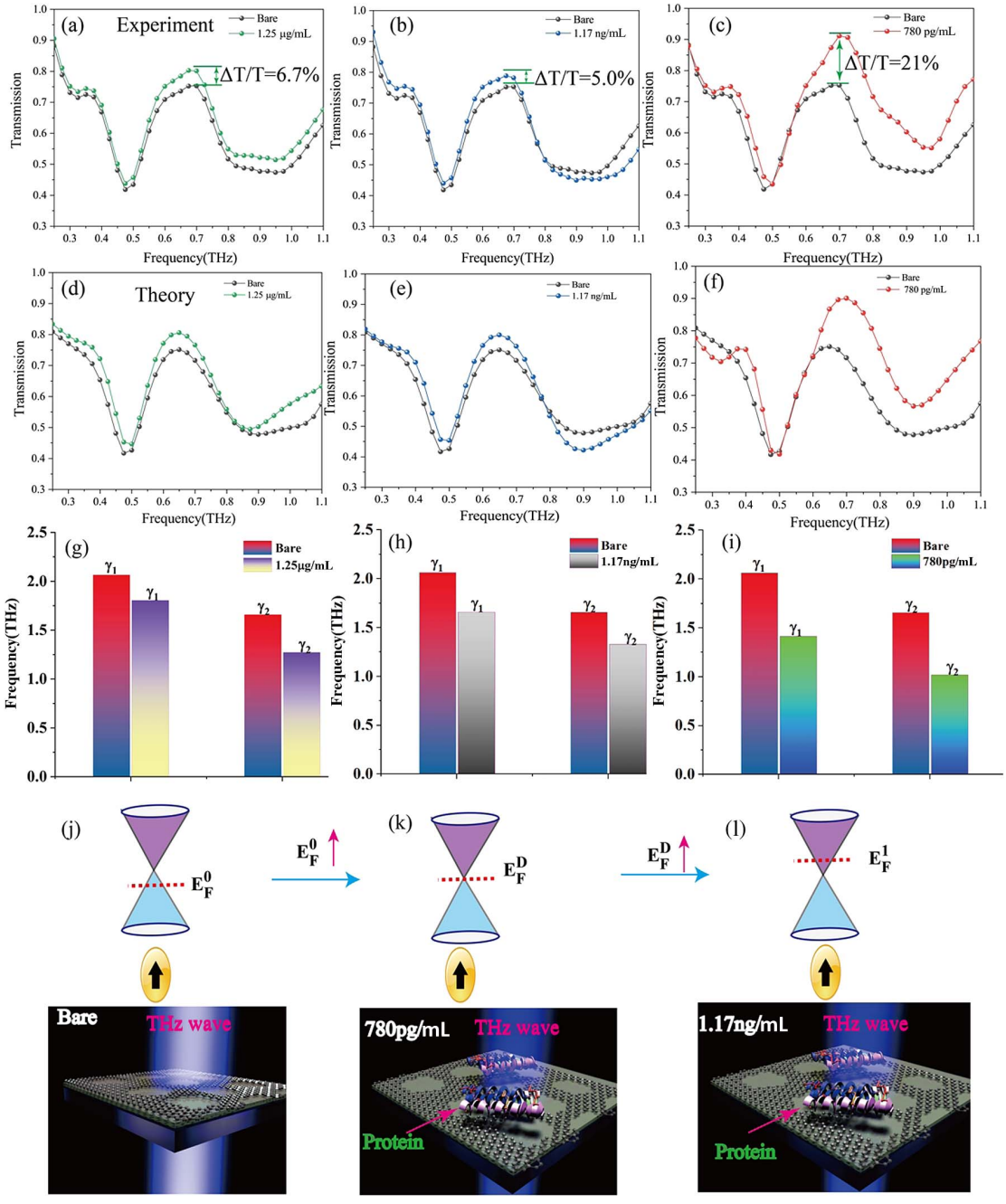

Fig. 3. Sensing performance of the HDOMM biosensor based on amplitude. (a)–(c) Experimental transmission spectra. (d)–(f) Corresponding theoretical fitted transmission spectra from (a)–(c). (g)–(i) Fitting parameters γ_1 and γ_2 as functions of sericin concentration. (j)–(l) Sensing mechanisms.

qualitatively detecting biosensor. This sensor was used to successfully detect sericin with a detection limit of 780 pg/mL. In addition, two abnormal THz responses were found: first, the transparency window with sericin is significantly higher than that for the bare HDOMM; second, $\Delta T/T$ for 1.25 μg/mL (highest concentration) is much lower than $\Delta T/T$ for 780 pg/mL (lowest concentration). To understand the internal mechanism of the two abnormal THz responses, the coupled harmonic oscillator model is used to fit the experimental transmission spectra for the HDOMM biosensor at sericin concentrations from 780 pg/mL to 1.25 μg/mL.

Figures 3(d)–3(f) present the theoretical fitted transmission spectra. The fitting results agree relatively well with the measurement. Figures 3(g)–3(i) show the fitting parameters γ_1 and γ_2 as functions of sericin concentration from 780 pg/mL to 1.25 μg/mL. Compared with those of the bare sample, both the radiative damping of the bright mode γ_1 and non-radiative damping of the dark mode γ_2 dramatically decrease under the influence of sericin. This is because introducing sericin changes the dielectric environment in the HDOMM, thus causing the reductions in γ_1 and γ_2. The combined results in Fig. 2(b) suggest that the conductivity of graphene has decreased. Therefore, the transmission amplitude significantly increases at the transparency window. The second abnormal THz response is more clearly explained by calculating $\Delta\gamma_1/\gamma_1 = [(\gamma_1^{\text{bare}} - \gamma_1^{\text{sericin}})/\gamma_1^{\text{bare}}] \times 100\%$ and $\Delta\gamma_2/\gamma_2 = [(\gamma_2^{\text{bare}} - \gamma_2^{\text{sericin}})/\gamma_1^{\text{bare}}] \times 100\%$.

Table 1. $\Delta\gamma/\gamma$ for Different Sericin Concentrations

Concentration of Sericin	$\Delta\gamma_1/\gamma_1$	$\Delta\gamma_2/\gamma_2$
780 pg/mL	32%	38%
1.17 ng/mL	20%	20%
1.25 μg/mL	13%	23%

The bigger $\Delta\gamma_1/\gamma_1(\Delta\gamma_2/\gamma_2)$ is, the more $\gamma_1(\gamma_2)$ is reduced. The results are shown in Table 1.

In Table 1, both $\Delta\gamma_1/\gamma_1$ and $\Delta\gamma_2/\gamma_2$ are maximum when the sericin concentration is at its minimum of 780 pg/mL. Such a sensing response is mainly caused by the unique bio-doping, which makes the initial E_F move to the Dirac point, leading to a sharp drop in the graphene conductivity. Figures 3(j)–3(l) show the sensing mechanisms of the HDOMM biosensor. CVD graphene is usually p-doped owing to the inevitable influence of impurities, defects, and disorder. The initial E_F slightly deviates from the Dirac point and is in the valence band, as shown in Fig. 3(j). The initial E_F is quite close to the Dirac point. As the 780-pg/mL sericin and the patterned graphene covalently bond, the initial E_F shifts from the valence band to the Dirac point, as shown in Fig. 3(k). The carrier density correspondingly decreases in the patterned graphene. Therefore, the conductivity decreases. This results in the observed marked enhancement of the transparency window. However, when the sericin concentration is 1.17 ng/mL, the initial E_F shifts from the Dirac point to the conduction band [see Fig. 3(l)]. The carrier density correspondingly increases, which enhances the conductivity. Therefore, the transparency window of the 1.17-ng/mL sericin is lower than that of the 780-pg/mL sericin. The results and theoretical analysis show that a substantial increase in the amplitude of the transparency window was achieved at the lowest sericin concentration; that is, ultrasensitive detection of sericin was achieved. The internal mechanism leading to this result is mainly that the E_F of graphene has moved to the Dirac point under the drive of the sericin, causing a dramatic change in the dielectric environment of the EIT coupling. Therefore, the conclusion drawn is that the ultra-sensitive sericin sensing is mainly caused by the E_F shifting to the Dirac point. The designed sensor is considered a Dirac-point-based biosensor. The sensitivity of this biosensor has been greatly improved compared with sensors of previous

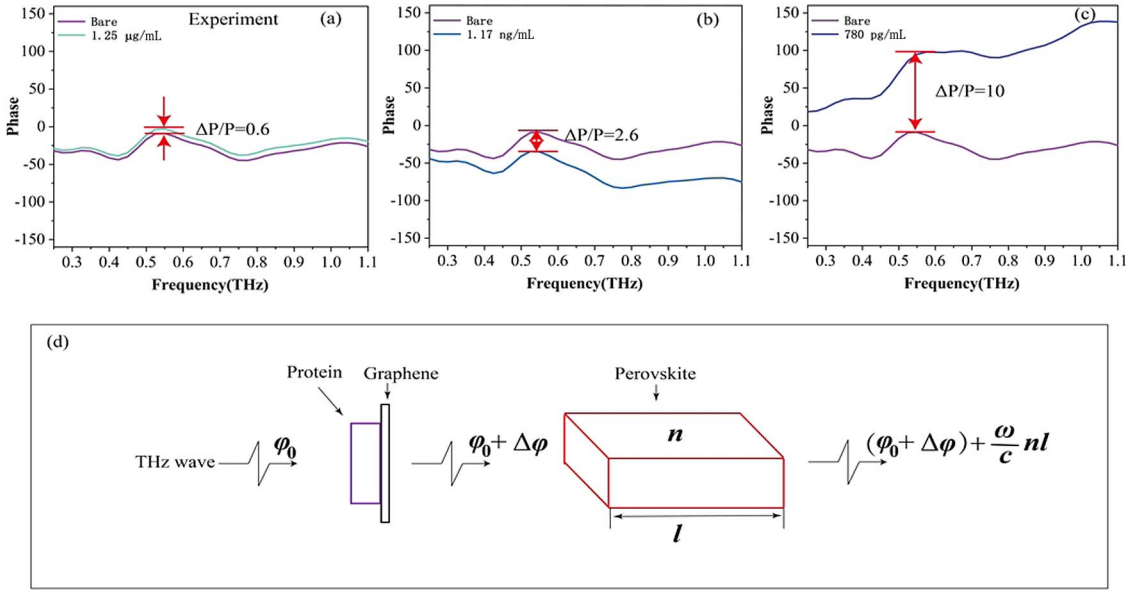

Fig. 4. Sensing performance of the HDOMM biosensor based on phase. (a)–(c) Experimental phase spectra for the HDOMM at sericin concentrations from 780 pg/mL to 1.25 μg/mL. (d) Role of perovskite in phase-based sensing.

Table 2. Comparison with Previous Works[a]

Sensors	Analytes	LOD	IBEMG	IDPBB
HDOMM	Sericin	780 pg/mL	No $\pi-\pi$ stacking	
Graphene + MS [42]	Fructose	100 ng/mL	No $\pi-\pi$ stacking	1.28×10^{2}
CNT + MS [15]	Chlorpyrifos methyl	10 ng/mL	$\pi-\pi$ stacking	1.28×10^{1}
Graphene + MS [42]	Chlorpyrifos methyl	20 ng/mL	$\pi-\pi$ stacking	2.56×10^{1}
Graphene + PI [43]	Chlorpyrifos methyl	130 ng/mL	$\pi-\pi$ stacking	1.66×10^{2}

[a]IBEMG, interaction between external molecules and graphene; IDPBB, improvement of Dirac-point-based biosensor; LOD, limit of detection; CNT, carbon nanotube; MS, metasurface.

works (Table 2). Here, we are based on the interaction between external molecules and graphene to compare the sensitivity of previous works. Sericin molecules have no benzene ring-like structures and are without π-electrons. Therefore, it cannot form $\pi-\pi$ stacking with graphene. First, we compare the no $\pi-\pi$ stacking case. In Table 2, we can find that the sensitivity of the Dirac-point-based HDOMM sensor is as much as two orders of magnitude higher than that of detecting fructose in Ref. [43]. In general, if an external molecule has a benzene ring-like structure with π-electrons, it strongly interacts with the π-electrons of graphene through $\pi-\pi$ stacking [42]. Therefore, the graphene-based sensor shows higher sensitivity to the external molecules containing π-electrons [42]. However, the sensitivity of the Dirac-point-based sensor to detecting sericin molecules without π-electrons is one order of magnitude higher than that of detecting chlorpyrifos methyl molecules that form $\pi-\pi$ stacking with graphene in previous work [15,42]. Furthermore, the sensitivity of the Dirac-point-based HDOMM sensor is as much as two orders of magnitude higher than that of the sensor (Graphene+PI) whose analytes contain π-electrons in Ref. [43]. In summary, the HDOMM sensor has higher sensing performance.

Figures 4(a)–4(c) show the experimental phase spectra for the HDOMM at sericin concentrations from 780 pg/mL to 1.25 μg/mL. The reference point of the phase spectra for the HDOMM with sericin is the corresponding phase in dry air. In Figs. 4(a)–4(c), the phase spectra of the HDOMM with sericin are significantly different from those for the bare HDOMM. The obvious change in the phase spectra also facilitates the qualitative sensing of sericin. To clarify the sensing effect further, it is defined as $\Delta P/P = |(P_{\text{sericin}} - P_{\text{bare}})/P_{\text{bare}}|$, where P_{sericin} (P_{bare}) is the phase at the transparency window with (without) sericin. From Figs. 4(a)–4(c), $\Delta P/P$ for sericin at 1.25 μg/mL (highest concentration) is 0.6, slightly lower than $\Delta P/P = 2.6$ at 1.17 ng/mL; however, this is much lower than $\Delta P/P = 10$ for sericin at 780 pg/mL (lowest concentration). The conclusion drawn from these results is that the HDOMM can serve as an ultra-sensitive qualitatively detecting biosensor. This sensor was used to successfully detect sericin with a detection limit of 780 pg/mL. As is the case for the phase-based sensing effect, and the phase spectra undergo the maximum change at the minimum sericin concentration of 780 pg/mL. The internal mechanism is also mainly that the E_F of graphene has moved to the Dirac point, causing a dramatic change in the dielectric environment. Figure 4(d) shows the mechanism through which perovskite facilitates phase-based sensing. When terahertz waves pass through graphene, φ_0 changes to $\varphi_0 + \Delta\varphi$ owing to the biological doping in graphene, where φ_0 is the initial phase of the terahertz wave, and $\Delta\varphi$ is the change in phase caused by the change in conductivity. After the terahertz waves pass through perovskite, $\varphi_0 + \Delta\varphi$ changes to $(\varphi_0 + \Delta\varphi) + (\omega/c)nl$, where ω is the frequency, c is the speed of light, n is the refractive index of perovskite, and l is the thickness of the perovskite. Because perovskite has a relatively high refractive index, Figs. 4(a)–4(c) show that the phase of terahertz waves $[(\varphi_0 + \Delta\varphi) + (\omega/c)nl]$ greatly changes with the sericin concentration. Therefore, perovskite plays an important role in phase-based sensing.

3. CONCLUSION

Ultra-sensitive and qualitative detection of sericin has been demonstrated using a new patterned graphene–PI–perovskite integrated terahertz metasurface as a platform for Dirac-point-based biosensing. The changes in amplitude and phase were used to successfully detect sericin with a detection limit of 780 pg/mL. The sensitivity of this sensor is as much as one order of magnitude higher than that of sensors in published works. The internal mechanism of ultra-sensitive biosensing was explained via simulation, coupled-harmonic-oscillator model fitting, and theoretical analysis of the changes in the graphene E_F. It was found that as 780-pg/mL sericin and the patterned graphene covalently bond, the initial E_F shifts from the valence band to the Dirac point. Correspondingly, the carrier density decreases in the patterned graphene, which decreases the conductivity. This results in marked enhancement of the transparency window. Thus, ultra-sensitive and qualitative detection of sericin was achieved. This work could lead to a wide range of ultra-sensitive and qualitative detection of biomolecules based on the Dirac-point-based biosensor.

APPENDIX A: EXPERIMENT

First, 1.3 mol/L PbI_2 and 0.3 mol/L CH_3NH_3I (MAI) were dissolved in 80 μL of a mixed solvent consisting of N,N-dimethylformamide and dimethyl sulfoxide at a volume ratio of 9:1. After that, the precursor solution was spin-coated on the metasurface at 6000 r/min for 15 s. Next, 60 μL of a MAI/isopropyl alcohol solution (35 mg/mL) was spin-coated on the wet film at 4500 r/min for 45 s. After spin-coating, the hybrid perovskite metasurface sample was transferred to a hot plate and pre-annealed at 70°C for 20 s in a glove box. Then the hybrid perovskite metasurface sample was annealed at 100°C for 30 min. After the spin-coating of perovskite on the metasurface was finished, a 2-μm-thick PI film was spin-coated on the $MAPbI_3$ film at 3500 r/min. When the drying of the PI film was completed, a 1 cm × 1 cm graphene sheet was carefully transferred

onto the dried PI film. Finally, the graphene was patterned. The patterning of the graphene was achieved in four steps [28]: (1) the metal mask was manufactured; (2) patterned zinc metal was sputtered on the uppermost layer of the graphene; (3) the HCl aqueous solution (0.02 mol/L) chemically reacted with zinc for 3 to 5 min to remove zinc while removing the graphene in contact with the patterned zinc; (4) after the first, second, and third Zn/HCl treatments, the patterned graphene was obtained. While the lowest detection limit of sericin was explored, 100-μL sericin solutions under different concentrations were dropped on the HDOMM biosensor, and the experimental test was performed after the water evaporation was completed.

APPENDIX B: MEASUREMENTS

An $8f$ confocal terahertz time-domain spectroscopy (THz-TDS) system was used for the measurements. Before the measurements, dry air was introduced to maintain a constant environment. The temperature was 27°C, and the humidity was 2.7% in the THz-TDS setup. An LED-optically pumped all-fiber femtosecond laser was used to generate a terahertz pulse. The wavelength of the laser center was at 1560 nm with a 100-fs pulse duration and 100-MHz repetition rate. The laser power was 100 mW during the measurements. The beam was split into two identical beams. One beam was used to generate the THz transient by exciting a biased photoconductive antenna, while the other served to detect the THz pulse. The THz time scan was 40 ps, and the spectral resolution was 40 GHz.

Funding. National Natural Science Foundation of China (61675147, 61701434, 61735010); Special Funding of the Taishan Scholar Project (tsqn201909150); Natural Science Foundation of Guangxi Province (ZR2020FK008); National Key Research and Development Program of China (2017YFA0700202, 2017YFB1401203); Qingchuang Science and Technology Plan of Shandong Universities (2019KJN001); Shandong Province Higher Education Science and Technology Program (J17KA087); Natural Science Foundation of Jiangsu Province (BK20180862); China Postdoctoral Fund (2019M651725); Natural Science Foundation of Shandong Province (ZR202102180769).

Disclosures. The authors declare no conflicts of interest.

Data Availability. Data underlying the results presented in this paper are not publicly available at this time but may be obtained from the authors upon reasonable request.

[†]These authors contributed equally to this paper.

REFERENCES

1. H.-T. Chen, W. J. Padilla, J. M. O. Zide, A. C. Gossard, A. J. Taylor, and R. D. Averitt, "Active terahertz metamaterial devices," Nature **444**, 597–600 (2006).
2. S. Han, M. V. Rybin, P. Pitchappa, Y. K. Srivastava, Y. S. Kivshar, and R. Singh, "Guided-mode resonances in all-dielectric terahertz metasurfaces," Adv. Opt. Mater. **8**, 1900959 (2020).
3. N. Yu, P. Genevet, M. A. Kats, F. Aieta, J.-P. Tetienne, F. Capasso, and Z. Gaburro, "Light propagation with phase discontinuities: generalized laws of reflection and refraction," Science **334**, 333–337 (2011).
4. C. X. Liu, F. Yang, X. J. Fu, J. W. Wu, L. Zhang, J. Yang, and T. J. Cui, "Programmable manipulations of terahertz beams by transmissive digital coding metasurfaces based on liquid crystals," Adv. Opt. Mater. **9**, 2100932 (2021).
5. T. C. Tan, Y. K. Srivastava, R. T. Ako, W. Wang, M. Bhaskaran, S. Sriram, I. Al-Naib, E. Plum, and R. Singh, "Active control of nanodielectric-induced THz quasi-BIC in flexible metasurfaces: a platform for modulation and sensing," Adv. Mater. **33**, 2100836 (2021).
6. T. Dong, S. Li, M. Manjappa, P. Yang, J. Zhou, D. Kong, B. Quan, X. Chen, C. Ouyang, F. Dai, J. Han, C. Ouyang, X. Zhang, J. Li, Y. Li, J. Miao, Y. Li, L. Wang, R. Singh, W. Zhang, and X. Wu, "Nonlinear THz-nano metasurfaces," Adv. Func. Mater. **31**, 2100463 (2021).
7. J. Li, C. Zheng, J. Li, G. Wang, J. Liu, Z. Yue, X. Hao, Y. Yang, F. Li, T. Tang, Y. Zhang, Y. Zhang, and J. Yao, "Terahertz wavefront shaping with multi-channel polarization conversion based on all-dielectric metasurface," Photon. Res. **9**, 1939–1947 (2021).
8. Q. Li, M. Gupta, X. Zhang, S. Wang, T. Chen, R. Singh, J. Han, and W. Zhang, "Active control of asymmetric Fano resonances with graphene–silicon-integrated terahertz metamaterials," Adv. Mater. Technol. **5**, 1900840 (2020).
9. S. H. Lee, M. Choi, T. T. Kim, S. Lee, M. Liu, X. Yin, H. K. Choi, S. S. Lee, C. G. Choi, S. Y. Choi, X. Zhang, and B. Min, "Switching terahertz waves with gate-controlled active graphene metamaterials," Nat. Mater. **11**, 936–941 (2012).
10. W. He, M. Tong, Z. Xu, Y. Hu, X. A. Cheng, and T. Jiang, "Ultrafast all-optical terahertz modulation based on an inverse-designed metasurface," Photon. Res. **9**, 1099–1108 (2021).
11. G. Rui, H. Hu, M. Singer, Y. J. Jen, Q. Zhan, and Q. Gan, "Symmetric meta-absorber-induced superchirality," Adv. Opt. Mater. **7**, 1901038 (2019).
12. J. Y. Suen, K. Fan, and W. J. Padilla, "A zero-rank, maximum nullity perfect electromagnetic wave absorber," Adv. Opt. Mater. **7**, 1801632 (2019).
13. N. Kundtz and D. R. Smith, "Extreme-angle broadband metamaterial lens," Nat. Mater. **9**, 129–132 (2010).
14. M. Gupta and R. Singh, "Terahertz sensing with optimized Q/V_{eff} metasurface cavities," Adv. Opt. Mater. **8**, 1902025 (2020).
15. R. Wang, W. Xu, D. Chen, R. Zhou, Q. Wang, W. Gao, J. Kono, L. Xie, and Y. Ying, "Ultrahigh-sensitivity molecular sensing with carbon nanotube terahertz metamaterials," ACS Appl. Mater. Interfaces **12**, 40629–40634 (2020).
16. H. M. Silalahi, Y.-P. Chen, Y.-H. Shih, Y.-S. Chen, X.-Y. Lin, J.-H. Liu, and C.-Y. Huang, "Floating terahertz metamaterials with extremely large refractive index sensitivities," Photon. Res. **9**, 1970–1978 (2021).
17. R. Zhou, C. Wang, Y. Huang, K. Huang, Y. Wang, W. Xu, L. Xie, and Y. Ying, "Label-free terahertz microfluidic biosensor for sensitive DNA detection using graphene-metasurface hybrid structures," Biosens. Bioelectron. **188**, 113336 (2021).
18. X. Yan, M. Yang, Z. Zhang, L. Liang, D. Wei, M. Wang, M. Zhang, T. Wang, L. Liu, J. Xie, and J. Yao, "The terahertz electromagnetically induced transparency-like metamaterials for sensitive biosensors in the detection of cancer cells," Biosens. Bioelectron. **126**, 485–492 (2019).
19. S. E. Harris, J. E. Field, and A. Imamoğlu, "Nonlinear optical processes using electromagnetically induced transparency," Phys. Rev. Lett. **64**, 1107–1110 (1990).
20. N. Liu, L. Langguth, T. Weiss, J. Kästel, M. Fleischhauer, T. Pfau, and H. Giessen, "Plasmonic analogue of electromagnetically induced transparency at the Drude damping limit," Nat. Mater. **8**, 758–762 (2009).
21. M. Chen, Z. Xiao, X. Lu, F. Lv, and Y. Zhou, "Simulation of dynamically tunable and switchable electromagnetically induced transparency analogue based on metal-graphene hybrid metamaterial," Carbon **159**, 273–282 (2020).
22. J. Li, J. Li, Y. Yang, J. Li, Y. Zhang, L. Wu, Z. Zhang, M. Yang, C. Zheng, J. Li, J. Huang, F. Li, T. Tang, H. Dai, and J. Yao, "Metal-

graphene hybrid active chiral metasurfaces for dynamic terahertz wavefront modulation and near field imaging," Carbon **163**, 34–42 (2020).
23. T.-T. Kim, H.-D. Kim, R. Zhao, S. S. Oh, T. Ha, D. S. Chung, Y. H. Lee, B. Min, and S. Zhang, "Electrically tunable slow light using graphene metamaterials," ACS Photon. **5**, 1800–1807 (2018).
24. H. Jung, J. Koo, E. Heo, B. Cho, C. In, W. Lee, H. Jo, J. H. Cho, H. Choi, M. S. Kang, and H. Lee, "Electrically controllable molecularization of terahertz meta-atoms," Adv. Mater. **30**, 1802760 (2018).
25. J. Zhang, J. Han, G. Peng, X. Yang, X. Yuan, Y. Li, J. Chen, W. Xu, K. Liu, Z. Zhu, W. Cao, Z. Han, J. Dai, M. Zhu, S. Qin, and K. S. Novoselov, "Light-induced irreversible structural phase transition in trilayer graphene," Light Sci. Appl. **9**, 174 (2020).
26. M. Yang, T. Li, J. Gao, X. Yan, L. Liang, H. Yao, J. Li, D. Wei, M. Wang, T. Zhang, Y. Ye, X. Song, H. Zhang, Y. Ren, X. Ren, and J. Yao, "Graphene–polyimide-integrated metasurface for ultrasensitive modulation of higher-order terahertz Fano resonances at the Dirac point," Appl. Surf. Sci. **562**, 150182 (2021).
27. H. Yao, X. Yan, M. Yang, Q. Yang, Y. Liu, A. Li, M. Wang, D. Wei, Z. Tian, and L. Liang, "Frequency-dependent ultrasensitive terahertz dynamic modulation at the Dirac point on graphene-based metal and all-dielectric metamaterials," Carbon **184**, 400–408 (2021).
28. A. Dimiev, D. V. Kosynkin, A. Sinitskii, A. Slesarev, Z. Sun, and J. M. Tour, "Layer-by-layer removal of graphene for device patterning," Science **331**, 1168–1172 (2011).
29. J. Feng, W. Li, X. Qian, J. Qi, L. Qi, and J. Li, "Patterning of graphene," Nanoscale **4**, 4883 (2012).
30. S. Shukla, S.-Y. Kang, and S. Saxena, "Synthesis and patterning of graphene: strategies and prospects," Appl. Phys. Rev. **6**, 021311 (2019).
31. H. Wang and D. H. Kim, "Perovskite-based photodetectors: materials and devices," Chem. Soc. Rev. **46**, 5204–5236 (2017).
32. A. S. Abhishek Kumar, M. Manjappa, S. Ramesh, Y. K. Srivastava, P. Agarwal, T. C. Sum, and R. Singh, "Excitons in 2D perovskites for ultrafast terahertz photonic devices," Sci. Adv. **6**, eaax8821 (2020).
33. H. Jing, Y. Zhu, R.-W. Peng, C.-Y. Li, B. Xiong, Z. Wang, Y. Liu, and M. Wang, "Hybrid organic-inorganic perovskite metamaterial for light trapping and photon-to-electron conversion," Nanophotonics **9**, 3323–3333 (2020).
34. M. Abdelsamie, T. Li, F. Babbe, J. Xu, Q. Han, V. Blum, C. M. Sutter-Fella, D. B. Mitzi, and M. F. Toney, "Mechanism of additive-assisted room-temperature processing of metal halide perovskite thin films," ACS Appl. Mater. Interfaces **13**, 13212–13225 (2021).
35. C. Tyznik, J. Lee, J. Sorli, X. Liu, E. K. Holland, C. S. Day, J. E. Anthony, Y. L. Loo, Z. V. Vardeny, and O. D. Jurchescu, "Photocurrent in metal-halide perovskite/organic semiconductor heterostructures: impact of microstructure on charge generation efficiency," ACS Appl. Mater. Interfaces **13**, 10231–10238 (2021).
36. Y. Wei, T. Ma, J. Chen, M. Zhao, and H. Zeng, "Metal halide perovskites for optical parametric modulation," J. Phys. Chem. Lett. **12**, 3090–3098 (2021).
37. M. Manjappa, Y. K. Srivastava, A. Solanki, A. Kumar, T. C. Sum, and R. Singh, "Hybrid lead halide perovskites for ultrasensitive photoactive switching in terahertz metamaterial devices," Adv. Mater. **29**, 1605881 (2017).
38. W. Tian, H. Zhou, and L. Li, "Hybrid organic-inorganic perovskite photodetectors," Small **13**, 1702107 (2017).
39. S. Xiao, T. Wang, T. Liu, X. Yan, Z. Li, and C. Xu, "Active modulation of electromagnetically induced transparency analogue in terahertz hybrid metal-graphene metamaterials," Carbon **126**, 271–278 (2018).
40. M. Yang, L. Liang, Z. Zhang, Y. Xin, D. Wei, X. Song, H. Zhang, Y. Lu, M. Wang, and M. Zhang, "Electromagnetically induced transparency-like metamaterials for detection of lung cancer cells," Opt. Express **27**, 19520–19529 (2019).
41. J. Gu, R. Singh, X. Liu, X. Zhang, Y. Ma, S. Zhang, S. A. Maier, Z. Tian, A. K. Azad, H.-T. Chen, A. J. Taylor, J. Han, and W. Zhang, "Active control of electromagnetically induced transparency analogue in terahertz metamaterials," Nat. Commun. **3**, 1151 (2012).
42. W. Xu, L. Xie, J. Zhu, L. Tang, R. Singh, C. Wang, Y. Ma, H.-T. Chen, and Y. Ying, "Terahertz biosensing with a graphene-metamaterial heterostructure platform," Carbon **141**, 247–252 (2019).
43. W. Xu, Y. Huang, R. Zhou, Q. Wang, J. Yin, J. Kono, J. Ping, L. Xie, and Y. Ying, "Metamaterial-free flexible graphene-enabled terahertz sensors for pesticide detection at bio-interface," ACS Appl. Mater. Interfaces **12**, 44281–44287 (2020).